SSRG International Journal of Electrical and Electronics Engineering
ISSN: 2348-8379/ https://doi.org/10.14445/23488379/IJEEE-V11I7P116

Volume 11 Issue 7, 185-198, July 2024

Original Article

Early Detection of Alzheimer's Disease: Leveraging Biomarker from FDG-PET Using Weighted SVM Clustering

Chintan R. Varnagar[1], Nirali N. Madhak[2], Prashant D. Maheta[3], Sanjay D. Bhanderi[4], Haresh M. Rathod[5]

[1,2,3,4,5]*Computer Engineering Department, Government Engineering College, Rajkot, Gujarat, India.*

[1]*Corresponding Author : chintan2287@gmail.com*

Received: 07 May 2024 Revised: 10 June 2024 Accepted: 07 July 2024 Published: 26 July 2024

Abstract *- Alzheimer's Disease (AD) is a progressive neurodegenerative disorder marked by cognitive decline, memory loss, and impaired reasoning, caused by the accumulation of amyloid-beta plaques and neurofibrillary tangles of tau protein. This study utilizes neuroimaging Fluorodeoxyglucose Positron Emission Tomography (FDG-PET) and structural MRI and clinical data from 1069 subjects acquired through the Alzheimer's Disease Neuroimaging Initiative (ADNI). Early-stage AD presents challenges for classification between Mild Cognitive Impairment (MCI) and Cognitively Normal (CN) individuals, as structural abnormalities are less pronounced, making sMRI-derived features less discriminative. However, functional connectivity disruptions in brain regions are notable in the early AD stages. This study investigates whether the metabolic brain assessment biomarker, Support Uptake Value Ratio (SUVR) from FDG-PET, can enhance classification performance between MCI and CN classes effectively or not. We introduced a novel weighted random SVM cluster, an ensemble method that outperforms single SVM classifiers by addressing issues of limited data and noise. Using the AAL3 Atlas, which provides finer subdivisions of brain regions (168 regions compared to AAL2's 90), we achieved a more detailed connectivity analysis. Employing rigorous pre-processing and a Stratified K-Fold Nested Cross Validation with k=5 and an 8:2 train-validation to test split ensured robust hyperparameter tuning and model selection to prevent overfitting and selection bias. The proposed method demonstrates good classification accuracy for MCI vs. CN and exhibits good ROC characteristics, indicating sensitivity to detect disruptive metabolic changes, highlighting its potential in early AD detection.*

Keywords *- Alzheimer's diseases, Quantified biomarkers of AD, Positron Emission Tomography, FDG-PET, Weighted SVM cluster.*

1. Alzheimer's Disease and Positron Emission Tomography (PET)

Alzheimer's Disease (AD) is a progressive neurodegenerative disorder characterized by cognitive decline, memory loss, and impaired reasoning. Pathologically, it is marked by the accumulation of amyloid-beta plaques and neurofibrillary tangles of tau protein, leading to synaptic dysfunction and neuronal death [1-3]. AD primarily affects the elderly, with its incidence increasing with age. Despite extensive research, the exact etiology remains unclear, involving complex interactions of genetic, environmental, and lifestyle factors [4, 5]. AD represents a significant public health challenge, necessitating ongoing research for effective diagnostics, treatments, and preventive strategies [6, 7].

PET is a medical imaging technique used to visualize and measure various physiological processes in the body. PET scans provide functional information by detecting and visualizing the distribution of a radioactive tracer that is injected into the patient.

In a PET study, the signal is generated through the detection of gamma rays emitted from a radioactive tracer injected into the patient. PET imaging is based on the principle of detecting pairs of gamma rays resulting from the annihilation of positrons emitted by the radioactive tracer. The following steps describe signal generation for PET studies.

1. Radiotracer Preparation: A radiochemist synthesizes a radiotracer, which is a biologically active molecule labelled with a radioactive isotope (commonly Fluorine-18 or Carbon-11). The most used radiotracer in PET studies for the purpose of neurodegenerative tracer is Fluorodeoxyglucose (FDG), a radioactive form of glucose.
2. Radiotracer Injection: The prepared radiotracer is injected into the patient's bloodstream. This is typically done

intravenously, ensuring that the radiotracer circulates through the body and reaches the target tissues.

3. Radiotracer Distribution: After injection, the radiotracer distributes throughout the body and gets accumulated in specific tissues or organs based on its biological properties. For instance, a glucose analogy like Fluorodeoxyglucose (FDG) will accumulate in areas with high glucose metabolism, such as active brain regions or tumour.
4. Positron Emission: Once it is inside the body, the radiotracer goes through radioactive decay, emitting positively charged particles called positrons (antielectrons) as it becomes stable.
5. Annihilation Event: Positrons emitted from the decaying radiotracer travel a short distance (usually a few millimetres) before encountering electrons in the surrounding tissues. When a positron meets an electron, they annihilate each other, resulting in the conversion of their mass into energy. This energy is released as two gamma photons.
6. Gamma Photon Detection: The two gamma photons produced by the annihilation event are emitted in nearly opposite directions (approximately 180 degrees apart). PET scanners, equipped with ring-like arrays of detectors, capture these photons. The coincidence detection system in the PET scanner identifies pairs of gamma photons that originate from the same annihilation event.
7. Image Reconstruction: The detected gamma photon pairs are processed by the PET scanner's computer system to reconstruct detailed images. Algorithms use information about the origin and trajectory of the photons to create cross-sectional images that represent the distribution of the radiotracer within the body. Advanced reconstruction techniques, such as iterative reconstruction, improve image quality and resolution. PET studies offer numerous benefits and, therefore, find its application in almost all clinical branches of medicine.

1.1. Benefits of PET Imaging Modality

1. Early Disease Detection: PET can detect functional and metabolic changes at the cellular level, allowing for early detection of diseases even before structural changes are evident. This is particularly useful in oncology and neurology.
2. Accurate Staging and Treatment Planning: PET is highly valuable in cancer staging, as it can assess the extent of tumour spread and detect metastases. It aids in planning appropriate treatment strategies.
3. Treatment Response Assessment: PET helps monitor the response to therapy, enabling clinicians to evaluate treatment effectiveness and adjust if necessary.
4. Differentiation of Benign and Malignant Lesions: PET can aid in distinguishing between benign and malignant lesions, reducing the need for invasive procedures and unnecessary surgeries.
5. Metabolic Mapping: PET provides functional information about metabolic activity, blood flow, and oxygen consumption in tissues and organs, helping researchers and clinicians understand organ function.
6. Non-Invasive: PET is a non-invasive imaging technique that minimises patient discomfort and reduces the risk of complications.

1.2. Radioactive Tracers

PET uses radioactive tracers, also known as radiotracers or radiopharmaceuticals, to visualize and measure physiological processes in the body. These radiotracers emit positrons, which interact with nearby electrons, resulting in the emission of gamma rays during the process of positron annihilation. The detection of these gamma rays allows PET scanners to create detailed images of the distribution and metabolism of the radiotracer within the body. Commonly used radioactive tracers in PET and their applications are as follows [8].

1. Fluorodeoxyglucose (FDG): FDG is the most widely used radiotracer in clinical PET imaging. It is a radioactive form of glucose, which is taken up by cells in proportion to their metabolic activity. FDG-PET is commonly used in oncology for cancer detection, staging, and treatment response assessment. Malignant cells, being more metabolically active, typically show increased FDG uptake compared to normal tissues.
2. Carbon-11 Methionine (11C-MET): 11C-MET is used in neuroimaging to study brain tumors and neurological disorders. It is taken up by cells that actively synthesize proteins, and its uptake in brain tumors is indicative of increased protein synthesis and cell proliferation.
3. Oxygen-15 Water (15O-H2O): 15O-H2O is used to study Cerebral Blood Flow (CBF) in the brain. It is a freely diffusible tracer that provides information about regional blood flow, helping in the evaluation of brain function and perfusion.
4. Nitrogen-13 Ammonia (13N-NH3): 13N-NH3 is used to assess myocardial blood flow in the heart. It is taken up by cardiac muscle cells in proportion to blood flow, making it valuable in diagnosing coronary artery disease and evaluating cardiac viability.
5. Rubidium-82 Chloride (82Rb): 82Rb is another tracer used for myocardial perfusion imaging. It has a similar application as 13N-NH3 in assessing myocardial blood flow and coronary artery disease.
6. Gallium-68 Dotatate (68Ga-Dotatate): 68Ga-Dotatate is used in neuroendocrine tumour imaging. It targets somatostatin receptors, which are often overexpressed in neuroendocrine tumours, allowing for their detection and localization.
7. Fluorine-18 Florbetapir (18F-AV-45, also known as Amyvid): 18F-AV-45 is used to visualize amyloid plaques in the brain, which are a hallmark of Alzheimer's

disease. It aids in diagnosing Alzheimer's and other neurodegenerative conditions.

8. Fluorine-18 Sodium Fluoride (18F-NaF): 18F-NaF is used for bone imaging to assess bone metastases and other bone-related diseases. It accumulates in areas of increased bone turnover, making it valuable for detecting bone lesions.
9. Copper-64 Pyruvaldehyde Bis (N4-methylthiosemicarbazone) (64Cu-ATSM): 64Cu-ATSM is being investigated for imaging hypoxic regions in tumors. It tends to accumulate in areas of low oxygenation, which can be useful for predicting tumor response to treatment.

Table 1. Overview of common radiotracers used in PET studies: targets and clinical applications

Radiotracer	Radioactive Isotope	Target	Clinical Applications
Fluorodeoxyglucose (FDG)	Fluorine-18 (18F)	Glucose metabolism	Oncology (tumors detection and monitoring), neurology (brain activity), cardiology (myocardial viability)
Florbetapir (Amyvid)	Fluorine-18 (18F)	Amyloid plaques	Alzheimer's Disease diagnosis
Flutemetamol (Vizamyl)	Fluorine-18 (18F)	Amyloid plaques	Alzheimer's Disease diagnosis
Choline (11C-Choline)	Carbon-11 (11C)	Cellular membrane synthesis	Prostate cancer imaging
Methionine (11C-Methionine)	Carbon-11 (11C)	Amino acid transport and protein synthesis	Brain tumor imaging, other cancers
Pittsburgh Compound B (PiB)	Carbon-11 (11C)	Amyloid plaques	Alzheimer's Disease research
Sodium Fluoride (NaF)	Fluorine-18 (18F)	Bone formation	Bone metastasis detection
Dopamine (18F-DOPA)	Fluorine-18 (18F)	Dopaminergic system	Parkinson's Disease and other movement disorders
Thymidine (18F-FLT)	Fluorine-18 (18F)	DNA synthesis	Cancer imaging (cell proliferation)
Annexin V (18F-Annexin V)	Fluorine-18 (18F)	Apoptosis	Imaging of cell death

1.3. Generation of the Signal Using FDG Radioactive Tracer

FDG tracer is a radioactive glucose that is used in PET scans. It is a radioactive form of glucose, a molecule that serves as the primary source of energy for cells in the body. FDG is a glucose analog, where the hydroxyl group at the C-2 position of the glucose molecule is replaced with a radioactive fluorine-18 atom.

The chemical structure of FDG is that of glucose, which allows it to be taken up by cells and metabolized similarly to glucose. The chemical composition is as follows.

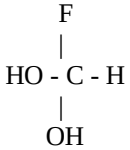

In this structure, "HO" represents a hydroxyl group (OH) that is replaced by a radioactive fluorine atom (F) at the C-2 position of the glucose molecule. FDG tracer is injected into the body through an Intra Venus (IV) method. The half-life of 18F is 110 minutes. This means that the radioactivity of the FDG tracer decays to half its original level in 110 minutes. The patient must wait for about an hour after the injection before the PET scan can be performed.

1.3.1. Uptake Mechanism

Once administered to the patient, FDG behaves similarly to glucose in the body. It is taken up by cells, particularly those with high metabolic activity. The uptake of FDG is mediated by Glucose Transporters (GLUTs) present on the cell membrane. Inside the cell, FDG undergoes phosphorylation, becoming FDG-6-phosphate, but it cannot be further metabolized due to the lack of a hydroxyl group at the C-2 position. As a result, FDG-6-phosphate accumulates within the cell, leading to the emission of positrons during radioactive decay.

1.3.2. Positron Emission and Imaging

FDG emits positrons (positively charged particles) as it undergoes radioactive decay. These positrons travel a short

distance in the surrounding tissues before encountering nearby electrons. Upon collision with electrons, positrons are annihilated, resulting in the emission of two gamma rays (photons) traveling in opposite directions.

PET scanners detect these gamma rays, allowing the reconstruction of 3D images that represent the distribution of FDG within the body. The intensity of the PET signal is proportional to the metabolic activity of the tissues, making FDG-PET a powerful tool for imaging and assessing various diseases and physiological processes [9].

When FDG tracer is injected into the body, it is taken up by cells that use glucose for energy. Abnormal cells use glucose less or more than normal cells, so they take up the amount of FDG tracer [10]. This allows PET scans to visualize abnormal cells that may not be visible on other imaging tests, such as X-rays, CT scans, or MRIs.

1.4. Biomarkers Derivable from FDG-PET

PET molecular imaging agents can elucidate multiple aspects of AD pathophysiology, including brain amyloidosis, tau protein accumulation, neuroreceptor alterations, metabolic abnormalities, and neuroinflammation. PET imaging serves as a critical tool for the early diagnosis of AD, disease staging, and monitoring responses to treatment.

Given the increasing emphasis on presymptomatic early diagnosis and disease-modifying interventions, PET molecular imaging agents offer an unparalleled capability to quantify the pathophysiological processes of AD, monitor disease progression, evaluate the engagement of therapies with brain molecular targets, and measure pharmacological responses. This study underscores the critical contributions of PET in elucidating brain molecular abnormalities associated with AD [11].

FDG-PET is a medical imaging technique that uses a radioactive tracer called FDG to measure glucose metabolism in various tissues and organs of the body. FDG-PET can provide valuable information about the functional activity and metabolism of cells. While FDG-PET itself does not measure specific biomarkers directly, it can indirectly reveal important metabolic and physiological information. Biomarkers that can be derived from FDG-PET, their usefulness and significance are discussed in the following paragraphs.

1. Standardized Uptake Value (SUV): SUV is a commonly used biomarker in FDG-PET imaging. It quantifies the uptake of FDG in tissues and provides information about their metabolic activity. SUV represents the concentration of FDG in a tissue region of interest normalized to the injected dose and the patient's body weight.
2. Tumor-to-Background Ratio (TBR): TBR is a biomarker that compares the FDG uptake in a tumor to the surrounding normal tissue or a reference region. It is often used to assess tumor metabolism and to differentiate between malignant and benign lesions.
3. Metabolic Tumor Volume (MTV): MTV measures the total volume of metabolically active tumor tissue. It identifies and quantifies the extent of tumor involvement by considering areas of increased FDG uptake. MTV can be useful for staging cancer, monitoring treatment response, and assessing tumor burden.
4. Total Lesion Glycolysis (TLG): TLG combines both the metabolic activity (SUV) and the Metabolic Tumor Volume (MTV) to provide a more comprehensive measure of tumor metabolism. TLG is calculated by multiplying the SUV by the MTV and can be useful for characterizing tumor aggressiveness and predicting patient outcomes.
5. Glucose Metabolic Rate (MRglu): MRglu represents the rate at which cells take up and metabolize glucose. It is a quantitative measure of tissue glucose metabolism and can provide information about the overall metabolic state of organs or tissues imaged with FDG-PET.

SUV is a quantitative metric employed in FDG-PET imaging to evaluate the uptake and concentration of the radioactive tracer FDG in tissues or lesions. This measure facilitates the quantification, standardization, and comparison of FDG uptake across different patients, brain regions (ROIs), and time points in longitudinal studies.

Additionally, it serves as a valuable tool for assessing treatment response. The SUV is calculated using the following formula:

SUV = (Tissue radioactivity concentration (Bq/mL) X Body weight (g)) / Injected FDG dose (Bq)

Where,

Tissue Radioactivity Concentration represents the concentration of FDG in the specific tissue or lesion being imaged and measured in Becquerels per milliliter (Bq/mL) and is obtained from the PET scan data.

Body Weight accounts for differences in FDG distribution based on body size and is measured in grams (g).

Injected FDG Dose the amount of FDG that was administered to the patient for the PET scan and is measured in Becquerels (Bq).

Further, an SUV is a dimensionless or a scalar quantity, meaning it has no units. It provides a standardized measure of FDG uptake that is independent of the injected dose and patient size, enabling direct comparisons between different patients and scans.

Hypometabolism, the areas of reduced glucose metabolism, can be detected by FDG-PET and patterns in these brain regions - such as the hippocampus, posterior

cingulate cortex, precuneus, and temporoparietal cortex, are typical early features of AD and can aid in the diagnosis of the disease.

2. Significance of FDG-PET in AD

It has been demonstrated that FDG-PET is a potential method for identifying and detecting metabolic and functional brain alterations in AD and MCI subjects, has been proven to be helpful for early detection and can be used for differential diagnosis of AD from other causes of dementia [12].

A novel and effective approach for the automatic classification of FDG-PET scans in subjects with AD and Frontotemporal Dementia (FTD) has been developed. Unlike previous methods that rely on principal component analysis and predefined regions of interest, this approach employs information gain and spatial proximity to cluster cortical pixels into empirically determined regions that are highly discriminative between AD and FTD.

These regions serve as attributes within a decision tree learning framework, achieving superior classification accuracy compared to existing methods. Our findings underscore the potential of this method in accurately distinguishing between AD and FTD patients, with significant implications for early detection and personalized treatment strategies in these neurodegenerative diseases [13].

In a multicenter study, researchers evaluated the accuracy of optimized procedures for FDG-PET brain metabolism and Cerebrospinal Fluid (CSF) classifications in predicting or excluding the conversion to AD dementia and non-AD dementias in individuals with MCI. The study included 80 MCI subjects who underwent neurological assessments, FDG-PET scans, and CSF measures at baseline, followed by clinical follow-ups. FDG-PET data were analyzed using a validated voxel-based Statistical Parametric Mapping (SPM) method, with resulting SPM maps classified by imaging experts based on disease-specific patterns.

Statistical analyses grouped the individual patterns into categories of AD dementia vs. non-AD dementia or FTD vs. non-FTD. The study found that FDG-PET SPM classification and CSF Aβ42 levels were the best predictors of conversion from MCI to AD dementia, while the "FTD" SPM pattern predicted conversion to FTD dementia.

Overall, FDG-PET SPM classification demonstrated higher accuracy in predicting progression to different dementia conditions in prodromal MCI, outperforming CSF biomarkers. These results highlight the significant role of FDG-PET SPM classification as a valuable biomarker for early detection and differential diagnosis of dementia conditions [14].

The study employed a novel deep learning method known as the "multi-feature kernel supervised within-class-similar discriminative dictionary learning algorithm" (MKSCDDL) to classify subjects with AD, MCI, and CN individuals. The model was trained on structural MRI (sMRI), FDG-PET, and florbetapir-PET data from the ADNI database.

The results demonstrated a significant improvement in classification accuracy compared to several other state-of-the-art machine learning algorithms [15]. The study employed a novel deep learning method known as Kernel-based Integrated Persistent Feature (KBI) to enhance the accuracy of analyzing persistent homology data for diagnosing AD.

Persistent homology is a mathematical technique used to study the topological structure of networks, and recent research indicates that altered network organization in the human brain can serve as a diagnostic tool for such conditions. Traditional methods for analyzing persistent homology data often lack accuracy.

The authors applied KBI to FDG-PET imaging data from 140 AD patients, 280 subjects with MCI, and 280 CN individuals. The results demonstrated that KBI could detect significant differences in network organization among AD patients, MCI patients, and healthy controls. Compared to other persistent homology-based and standard graph-based measures, KBI showed more significant group differences and better classification performance, suggesting its potential as an effective preclinical AD imaging biomarker [16].

The study compared the diagnostic accuracy of CSF biomarkers and PET for diagnosing early-stage AD. Amyloid deposition in nine brain regions was assessed using FDG-PET, and CSF was analyzed with INNOTEST and EUROIMMUN ELISAs.

The results indicated that both CSF biomarkers and amyloid PET were highly accurate in diagnosing early AD, with no significant difference in diagnostic accuracy between the two modalities. Furthermore, combining CSF and PET did not enhance diagnostic accuracy beyond what was achieved by either method alone [17].

3. Materials and Methods

3.1. Data Selection

The participants whose FDG-PET and T1w sMRI, both scans (modalities) were available at baseline, were included in this study. Details, distribution, demography of subjects, and their clinical assessment scores (MMSE & CDR) used in this section are mentioned in Table 2. An additional FDG-PET modality-specific preprocessing step that was applied to neuroimaging data used in this study is described in section 3.4.

Table 2. Demographic and clinical characteristics of subjects from the ADNI Cohort

	CN	sMCI	pMCI	AD	Total
# of subjects/images	404	166	177	322	1069
Gender (# male/# female)	202/202	98/68	104/73	177/145	581/488
Age in years mean [min; max]	74.2 [59.8; 89.6]	74.4 [55.9; 91.4]	74.3 [48.1; 88.3]	75.8 [55.1; 91.4]	74.6 [48.1; 91.4]
MMSE (mean, [min; max])	29 [24; 30]	28 [23; 30]	26 [23; 30]	23 [19; 26]	-- [19; 30]
CDR (mean, [min;max])	0.34 [0; 1]	1.26 [0.5; 1]	2.08 [0.5; 2]	2.69 [1; 3]	0.92 [0; 3]

CN - Cognitively Normal / Healthy Control.
sMCI - Stable MCI; (subjects were tracked/followed up and did NOT progress to AD in 24 months from their first visit and visit at 24 Months)
pMCI - Progressive MCI (subjects were tracked/followed up, and they had progressed to AD in 24 months. i.e. between the time of their first visit to the subsequent 24 Months)
AD - Alzheimer's Disease patient.

Every subject belonging to the MCI group is categorized (falls) into either sMCI or pMCI class.

People with normal cognition did not have memory problems, but people with MCI and AD are reported with some deficits and decline. MMSE and CDR score for each category of the subjects is mentioned in Table 2 as a tuple in {mean, [minimum; maximum]} format.

Figure 1 illustrates the distribution of data across three classes of interest. Meanwhile, Figure 2 depicts the age distribution (in years) of the subjects within these classes.

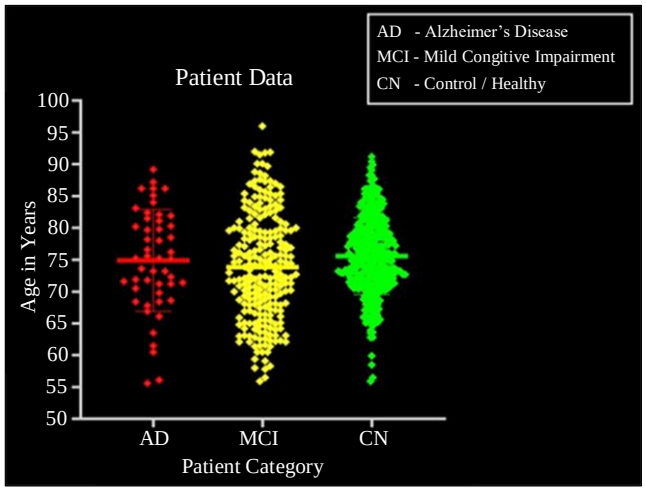

Fig. 1 Age distribution of subjects across different classes in the ADNI dataset

This study utilized standardized, Quality Controlled (QC-passed), 3-Dimensional Magnetization Prepared Rapid Gradient Echo (3D-MPRAGE) files to mitigate data preprocessing and acquisition variations as outlined in [18].

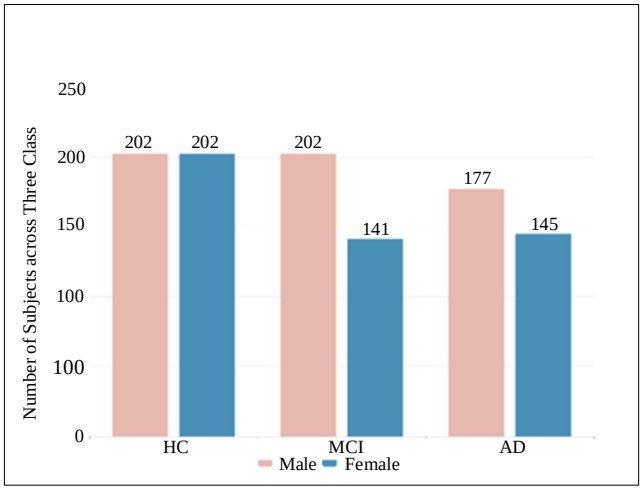

Fig. 2 Dataset distribution Vs Number of subjects taken from each Cohort (class)

These files underwent essential preprocessing steps, including Gradwarping for correcting spatial distortions due to gradient non-linearity, intensity normalization to address B1 non-uniformity, N3 correction for sharpening histogram peaks to reduce intensity non-uniformity caused by wave or dielectric effects and scaling for gradient drift. Data from ADNI, quality assured by the Mayo Clinic and hosted at the LONI database, includes detailed information on specific preprocessing corrections applied to each image or series of scans under consideration. The study adhered to the Brain Imaging Data Structure (BIDS) [19], a standardized framework for organizing and sharing neuroimaging data. BIDS ensures a consistent and well-defined structure for storing various types of brain imaging data, such as sMRI, fMRI, DWI, and PET data, facilitating easier analysis and data sharing across diverse research groups and software platforms.

By adhering to the BIDS format, this study aims to ensure that the data is organized in a consistent and standardized manner. This facilitates data sharing, integration of data across multiple sites, collaboration, and reproducibility in the field and across research groups and labs. The raw neuroimaging data acquired from ADNI for FDG-PET and sMRI both is converted into BIDS format.

3.2. Conversion of Raw Data to Standard Format (BIDS)

The raw data available from the scanner is converted using the following steps for the reasons and to avail benefits mentioned above into BIDS [19] format.

1. Obtain a List of Subjects and Sessions: Start by acquiring the list from the ADNIMERGE spreadsheet.
2. Compare Available Scans: Compare the scans to the list of subjects and sessions.
3. Multiple Scans for Subject-Session Pair: Determine if multiple scans exist for a specific subject-session pair.
4. Select Single Scan for Conversion:
   If the modality is T1:
   - Preferred Scan: Check if a preferred scan is identified in MAYOADIRL_MRI_IMAGEQC_12_08_15.csv. If so, select it.
     - Higher Quality Scan: If no preferred scan, choose the higher quality scan based on MRIQUALITY.csv.
     - First Scan: If no quality control information is available, choose the first scan.
     - For other modalities, select a single scan.
5. Use Specific Images for sMRI: If the modality is sMRI, use gradwrapped and B1-inhomogeneity corrected images.
6. Use Averaged Images for FDG-PET: For FDG-PET scans, use the co-registered and averaged images across time frames.
7. Discard Scans That Fail QC: Discard scans that fail quality control.
8. Convert to BIDS Format: Convert the selected imaging data to BIDS format.
9. Generate BIDS Folder Structure: Create the folder structure with subject subfolders, session subfolders, and modality subfolders within each session subfolder.

3.3. Data Acquisition, Protocol Parameters and Configuration of FDG-PET Data

The experimental neuroimaging (FDG-PET and sMRI), clinical and study data used in this study were acquired from the ADNI database. The ADNI FDG-PET protocol consists of a dynamic 3D scan of six five-minute frames (6*5) = 30 mins, 30 to 60 minutes post-injection with a radiation dose of FDG:185 MBq (becquerel) equivalent to 5 millicurie (mCi). Imaging sequence parameters for FDG-PET neuroimaging data and the associated values for it are mentioned in Table 3.

Table 3. Acquisition protocol parameters and corresponding values for FDG-PET imaging

Scanning Modality	Fluorodeoxyglucose (FDG) Positron Emission Tomography (PET)
Radiotracer	[18F]-Fluorodeoxyglucose (FDG)
Scan Duration	Six, five-minute frames (6*5) = 30 mins
Image Matrix	128 x 128 x 64
Voxel Size	2 x 2 x 2
Injection Dose	185 MBq = 5 millicurie (mCi) of FDG
Injection Time	30 to 60 minutes before the scan
Injection Protocol	IV bolus over 1 minute
Scanning Protocol	Dynamic 3D acquisition

3.4. Preprocessing of FDG-PET Data

The raw data, FDG-PET scans, acquired from ADNI is converted into BIDS [21] format, as mentioned in section 3.2. sMRI (T1w) imaging data is also converted into the MNI space. Following (FDG-PET modality specific) pre-processing steps were performed manually and, in the order /sequence mentioned here, on the (FDG-PET) data to remove artifacts and possible noise and to transform it into standard format and space so that registration can be done. This pre-processing has also contributed to improving the overall accuracy of the ML algorithm as well, and it is represented graphically in Figure 3.

1. The PET preprocessing pipeline utilized SPM12 [20] and PETPVC8 [21] for Partial Volume Correction (PVC).
2. Non-brain areas were removed using SynthStrip [22] utility, done earlier in section 3.6
3. Register the PET image to the corresponding T1w image in native space using the co-register method/module in SPM.
4. A PVC step with the Regional Voxel-Based (RBV) method has been performed, using tissue maps from the T1w in native space as input regions.
5. Register PET image into MNI space using the transformation mentioned in section 3.7 as for corresponding T1w.
6. In MNI space, the PET image is intensity normalized based on a reference region (eroded pons for FDG-PET) to generate a Standardized Uptake Value Ratio (SUVR) map.
7. The resulting masked SUVR images are in a common space, providing voxel-wise correspondence across subjects.

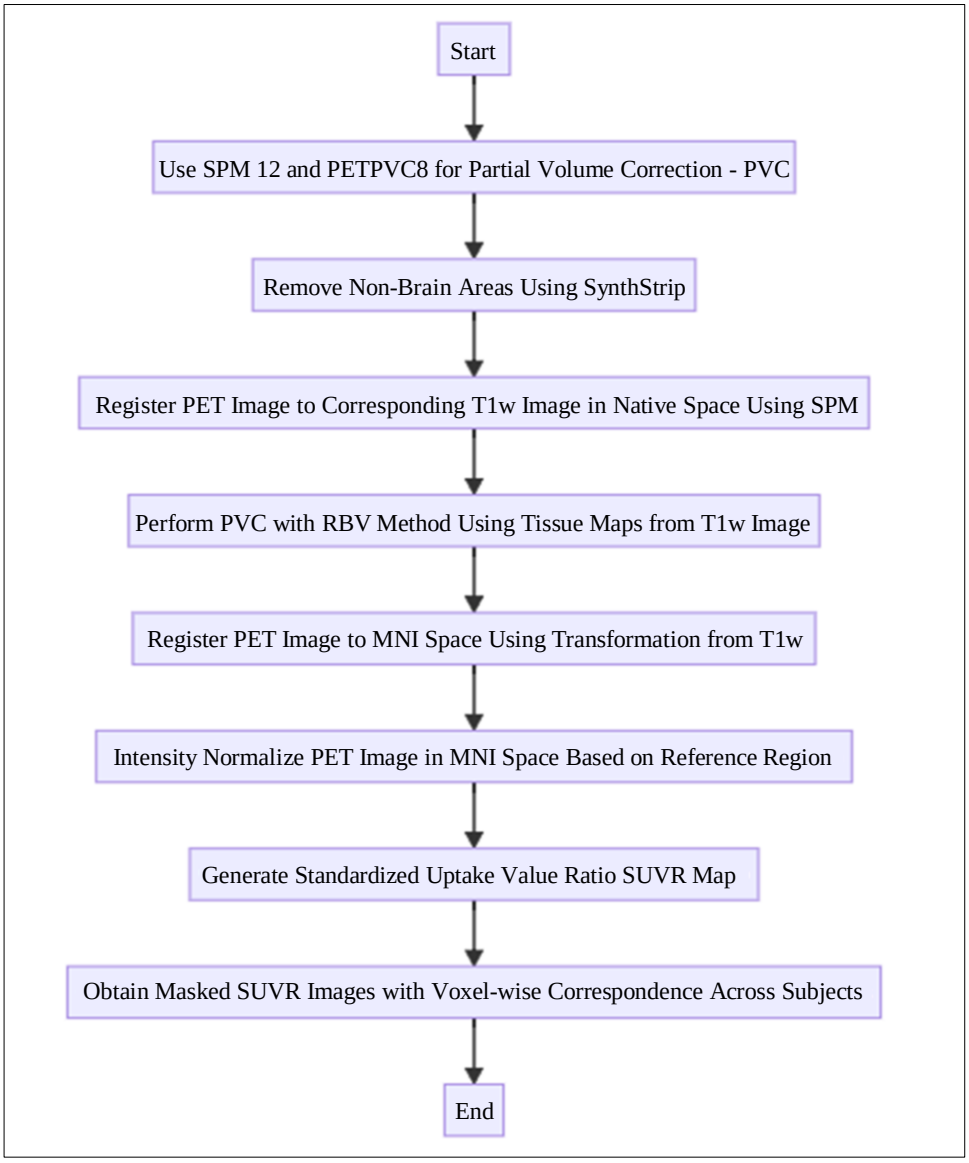

Fig. 3 PET preprocessing pipeline

4. Results and Discussion

In the later or advanced stage of AD, structural loss of neurons leading to brain atrophy can easily be detected by sMRI modality and thus, Convolutional Neural Network (CNN) and volumetric brain morphological studies can differentiate AD vs CN with very good accuracy and has excellent Receiver Operating Characteristic & Area Under Curve (ROC-AUC) characteristics. However, in the early stages of the disease, i.e. MCI stage, those structural abnormalities and associated atrophy are not so significant, and thus, it makes the classification of MCI vs CN challenging. In this scenario sMRI derived biomarkers and associated features are not so discriminative.

In the initial stage of the diseases, the uptake mechanism of glucose reflecting metabolic disruptive changes in the form of hypometabolism is seen much prior, in many cases up to one decade prior, as compared to any atrophy-related structural changes, accessible through sMRI [14, 16]. These disruptive changes are gross indicators of disturbance in the brain connectivity, cohesiveness, and coordination within or between different brain regions or areas and thus have the potential to be used as a biomarker and feature for the ML model to predict with good accuracy for MCI vs CN.

SUVR, a biomarker derived from FDG-PET neuroimaging data, is sensitive towards detecting underlying metabolic and physiological information by multiple researchers and is outlined in sections 1 and 2. FDG-PET aims to measure or quantify these hypometabolism related differences during its early stages and effectively as well. With this hypothesis, whether these FDG-PET derived metabolic

changes can give a better overall performance in differentiating MCI vs CN classes or not, in this research, we have extracted two types of features from FDG-PET neuroimaging data: 1) voxel-wise and 2) regional features. Voxel-wise features correspond to the signal value received in the form of SUVR, obtained from all (each) voxel in the brain and regional features correspond to the *average signal* computed in a set of ROIs in the context of AAL3 [23] atlas. The classification was performed using SUVR as a biomarker, reflecting scikitmetabolic activities.

In the AAL3 atlas, the brain was divided into 80 ROIs in each cerebral hemisphere (left and right), totaling 160 ROIs; additionally, 8 midline structures were included, resulting in a total of 168 ROIs. AAL-3 offers improvements over its earlier versions by providing finer brain parcellation, enabling detection and localization of signals from smaller brain areas, and avoiding signal deterioration due to averaging and supporting smaller voxel sizes as well.After completing a series of data preprocessing steps as mentioned in section 3.4, the SUVR value averaged over each ROI, defined in the context of the AAL3 atlas, is retrieved from each ROI for all the subjects, resulting in 168 SUVR values per subject, which is to be used as the feature by ML model later for predicting a class label.

The experiments are performed on the datasets described in Section 3.1. and is mentioned in Table 2, consisting of 1069 subjects. The composition of the data derived from the ADNI dataset for the classification task performed here, i.e., MCI vs CN, has 273 (M:161, F:112) subjects labelled MCI and 404 (M:161, F:161) subjects labelled as CN. Out of an available total of 747 subjects, 595 (80%) matched w.r.t. available demographic details are used in training/validation and the remaining 152 (20%) subjects are used for testing and performance evaluation of the model.

The dataset was partitioned into three subsets: a training set, a validation set, and a testing set. The training set was employed to train the model, while the validation set was utilized for hyperparameter tuning and decision-making regarding model selection. The testing set remained untouched until the final stage, where it was exclusively used for calculating final metrics and conducting comparative analyses between models. Figure 4 visually depicts the train-validation-test strategy implemented in this study to develop and evaluate the model.

The train-validation split enables simultaneous hyperparameter tuning and model selection/configuration to prevent overfitting and selection bias. The discovered hyperparameters are then applied to reconfigure the final model using the entire train-validation dataset for making predictions. The classification task focused on distinguishing between MCI and CN subjects. To ensure generalizability and prevent overfitting, we employed the "Stratified K-Fold Nested Cross-Validation" technique with k=5, where the train-validation to test split ratio was 8:2.

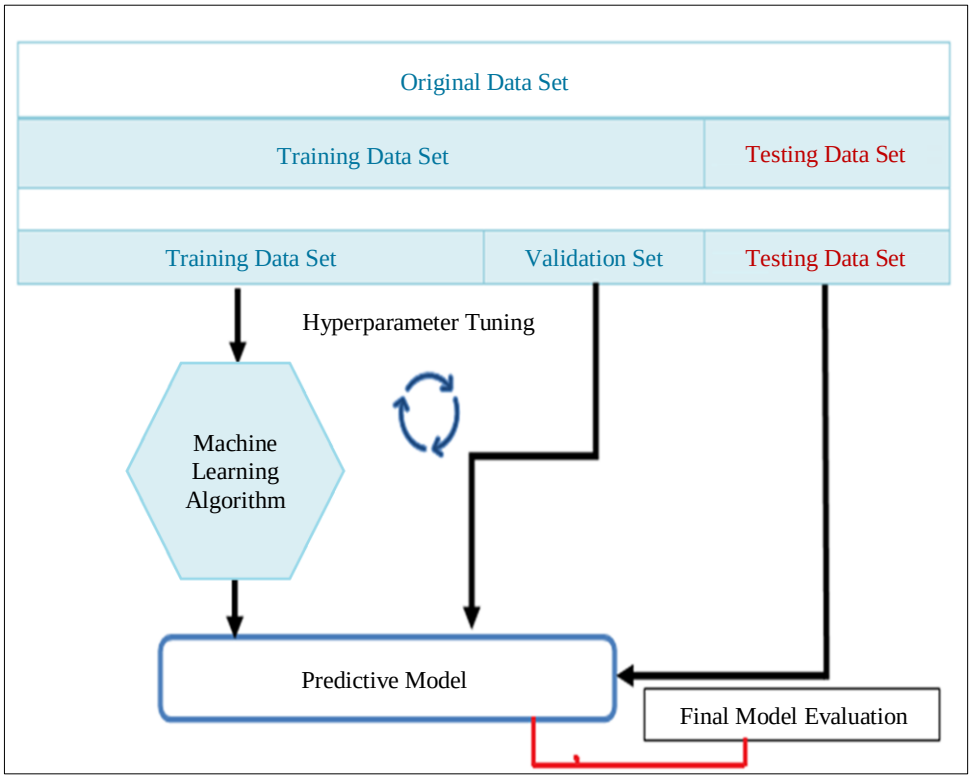

Fig. 4 Strategy for model building & configuration

This approach ensures that each fold of the dataset used for model training maintains a balanced proportion of positive and negative classes, accounting for all demographic details as outlined in Table 2.

In the nested cross-validation procedure described earlier, the inner loop (performed using scikit-learn's [24] GridSearchCV() maximizes the score by training a model on each training set and then optimizing (hyper) parameters based on the validation set. In the outer loop, the generalization error is assessed by averaging scores from the test set across multiple dataset splits.

ML methods were widely used for pattern recognition and SVM based model has demonstrated good performance in classifying high dimensional neuroimaging data with good efficacy. At the same time, a single SVM is not found to be stable, suffers from low accuracy, and often represents underfitting.

In this study, we implemented an approach capable of automatically extracting high-dimensional features. Specifically, we proposed and employed the 'random SVM cluster' method. This method offers several advantages: 1) Enhanced robustness through the integration of multiple SVMs and 2) Improved efficiency via the reinforcement of strong SVM base classifiers using a weighted approach. The FDG-PET neuroimaging data used in this study underwent the preprocessing steps detailed in Section 3.4 and utilized SUVR as a biomarker feature.

The complete pipeline of the proposed model, detailing the steps to derive class labels, is summarized and visually represented in Figure 5.

1) The entire available dataset is divided into 5 folds, as mentioned earlier, and the same training (N1) – validation (N2) – testing (N3) splitting strategy is applied.
2) At each (n^{th}) iteration – the number of samples/subjects is randomly selected from the training set N1, and some d-dimensional feature is randomly selected from 168-dimensional sample feature space to construct an SVM classifier. This avoids any a-priori features derived from previous knowledge directly fed into the model.
3) Thus, a single (and each) SVM is formed using randomly selected samples and features, using the Radial Basis Function (RBF) as a kernel function and yields different decision boundaries (hyperplane) and thus, it has a different classification performance and so aids to mitigate overfitting in the model.
4) The accuracy of each SVM on the training dataset is evaluated by sorting it in descending order (highest-to-lowest); the SVMs with the highest performances make more contributions to the overall performance, and the features used by these SVMs are referred to as "optimal features".
5) The performance of this ML model is evaluated by feeding a test sample to the trained model, the total amount of votes belonging to class '*a'* is denoted by S_a as follows.

$$\boldsymbol{S(a) = \sum_{i=1}^{n} \; I\,(f_i(x) = a)\; x\; W_i} \qquad (1)$$

Where,
x - Sample from the test set,
$f_i(x)$ - A class label predicted by i^{th} SVM from the test set,
W_i - Weights used from the validation test for hyperparameter tuning.

Cost parameter c for each SVM is set to Inf and RBF kernel with a bandwidth $\sigma = 3$.

The label with the greatest cumulative number of votes represents the final predicted label A of the test sample. Classification accuracy P_{true} is identified as follows,

$$\mathbf{P_{true}} = \frac{\mathbf{T_{true}}}{\mathbf{T}} \qquad (2)$$

Where,
T_{true} = Number of test samples that were correctly classified, and
T = Total number of samples in the test set.

The overall approach, this design has explored the space ranging from 1 to 40 (# of SVM) and found that the single SVM's accuracy ranges from 0.58 to 0.85; however, the Balanced Accuracy (BA) of such a weighted random SVM cluster achieved here is 84.87%. Interpretation leads to the conclusion that the random SVM cluster can make up for the unpredictability and poor accuracy of a single classifier. To derive what numbers of SVMs would be sufficient and enough (i.e., could reach global maxima of accuracy) in the proposed weighted random SVM cluster and to establish that betterment in the result achieved is not because of randomness indeed; also, the model does not represent the case of overfitting, and this approach can generalize well in the general scenario as well, the effect of the number of SVMs in random SVM cluster and corresponding balanced accuracy achieved there on is evaluated.

The number of base SVMs in the cluster when crosses 18, the training accuracy becomes stable, and it becomes range bound when SVMs are in the range of 18 to 25. It has been observed through the experiments that adding excessive base SVM classifiers after reaching global maxima does not contribute to increasing the overall performance, and it remains range-bound. Further, it adds experimental training overhead and even leads to overfitting. So, we have used 18 base SVMs in the final model. Further, the total number of features available is 168 per subject, which is manageable and hence does not require identifying "optimum features".

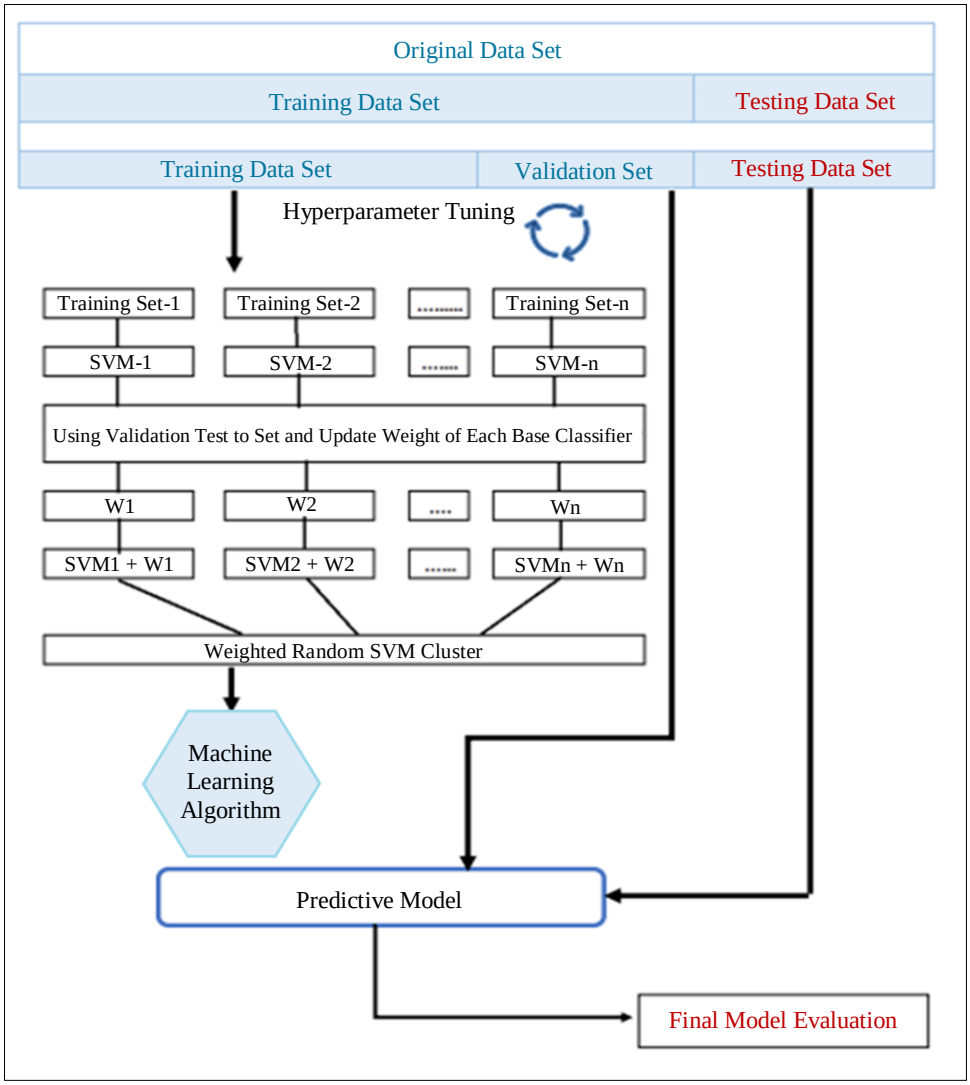

Fig. 5 The overall approach, train-test split, model evaluation, and overall system/model architecture of weighted random SVM cluster

The confusion matrix summarizes the classifier's predictions compared to the actual class labels. It includes True Positives (TP), True Negatives (TN), False Positives (FP), and False Negatives (FN), providing a comprehensive evaluation of classifier performance.

4.1. Accuracy

The overall correctness of the classifier, i.e., "the ratio of correctly recognized samples to the total number of tested samples," is also known as Balanced Accuracy (BA) and is calculated as follows.

$$\text{Accuracy} = \frac{\text{TP} + \text{TN}}{\text{TP} + \text{FP} + \text{FN} + \text{TN}}$$

4.2. Precision

The ability of the classifier to correctly identify positive instances (class) given by,

$$\text{Precision} = \frac{\text{TP}}{\text{TP} + \text{FP}}$$

4.3. Recall

The ability of the classifier to correctly identify all positive instances (class), also known as Sensitivity (SEN) or True Positive Rate (TPR), is given by,

$$\text{Recall} = \frac{\text{TP}}{\text{TP} + \text{FN}}$$

4.4. Specificity (SPE)

The ability of the classifier to correctly identify negative instances (class), also known as Ture Negative Rate (TNR), is given by,

$$\text{Specificity} = \frac{\text{TN}}{\text{TN} + \text{FP}}$$

4.5. F1-Score

The F1 score is the harmonic mean of precision and recall. It provides a balanced measure that considers both precision and recall and is given by,

$$F1 = \frac{2 * (\text{precision} * \text{recall})}{(\text{precision} + \text{recall})}$$

The proposed approach achieved a maximum Balanced Accuracy (BA) of 84.87% for the classification task of MCI versus CN using FDG-PET neuroimaging data. Detailed performance metrics and other parameters are reported in Table 4, with graphical representations provided in Figure 6, and ROC-AUC characteristics are represented in Figure 7.

Table 4. Performance evaluation of FDG-PET modality for MCI Vs CN

ML Model – Weighted Random SVM Cluster	Features Used	MCI Vs CN			
		BA	SEN	SPE	F1
	SUVR	84.87	85.0	84.78	83.60

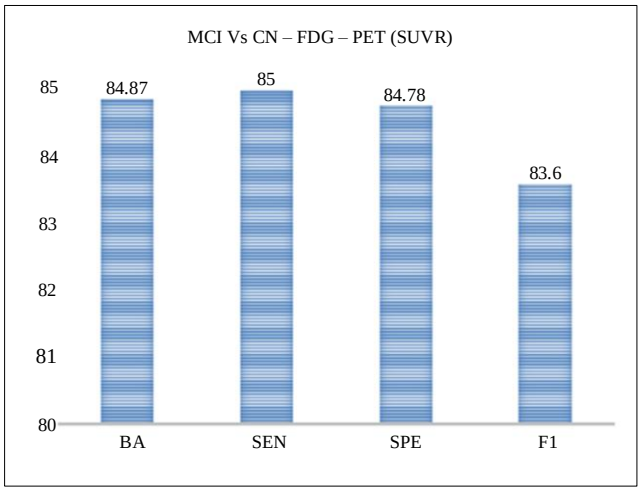

Fig. 6 Classification accuracy of SUVR biomarker from FDG-PET for MCI Vs CN

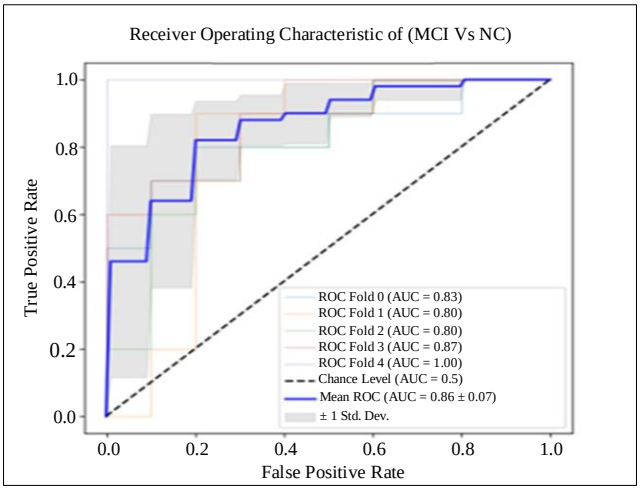

Fig. 7 ROC (mean and fold wise) and AUC curve for MCI Vs CN

5. Conclusion

PET has been proven to be a reliable tool for mapping the brain's metabolism and can often detect disruptive changes within the brain before any structural atrophies are accessible through sMRI data. This makes it a good modality to derive biomarkers from and use this to build ML models to predict class labels. Biomarker SUVR, derived from FDG-PET, provides an efficient approach to measuring, analysing and detecting disruptive changes by applying ML methods and models. Many single SVM algorithms that deal with neuroimaging data have poor precision for classification because of limited availability and noise in the data. To address these issues, we have introduced the novel weighted random SVM cluster, which is the weighted ensemble of individual SVM and does a better job of classifying than a single SVM classifier.

The AAL3 Atlas, which was used to measure brain connectivity, has 168 regions, which have more anatomical regions than its predecessor, AAL2 (90), or AAL. This makes it easier to divide the brain into smaller parts (fine-grain subdivisions) and facilitates accessing metabolic alterations very early, allowing for a better study of brain metabolism-related alterations.The proposed methods developed here yield good classification accuracy for MCI vs CN task and have demonstrated good ROC/AUC curves, suggesting that it has the potential to access subtle and minor changes within the brain and is sensitive towards detection of MCI subjects. The training and test accuracy achieved indicates that the model is stable, effective and optimum. The quantified value of SUVR can aid clinicians in better diagnosis and build trust in the CAD system/model.

Acknowledgments

Supercomputing facility (PARAM- SHAVAK) provided by Government Engineering College Rajkot in association with CDAC and GUJCOST.

Author Contributions

Conceptualization: C. Varnagar, S. Bhanderi. Data curation: N. Madhak, P. Mehta. Formal analysis: H. Rathod. Investigation & Implementation: C. Varnagar, N. Madhak. H. Rathod. Resource Pooling & Management: P. Mehta. Software and Result Validation: C. Varnagar, N. Madhak. Visualization: S. Bhanderi. Writing-original draft: C.

Varnagar, P. Mehta. Writing-review and editing: N. Madhak, C. Varnagar, P. Mehta, H. Rathod. All authors have read and approved the final manuscript.

Availability of data and materials

Data used in preparation of this research were obtained from the Alzheimer's Disease Neuroimaging Initiative (ADNI) database (adni.loni.usc.edu). As such, the investigators within the ADNI contributed to the design and implementation of ADNI and/or provided data but did not participate in the analysis or writing of this report. A complete listing of ADNI investigators can be found at: http://adni.loni.usc.edu/wp-content/uploads/how_to_apply/ADNI_Acknowledgement_List.pdf

References

[1] Kejal Kantarci et al., "White-Matter Integrity on DTI and the Pathologic Staging of Alzheimer's Disease," *Neurobiology of Aging*, vol. 56, pp. 172-179, 2017. [CrossRef] [Google Scholar] [Publisher Link]

[2] Alberto Serrano-Pozo et al., "Neuropathological Alterations in Alzheimer Disease," *Cold Spring Harbor Perspectives in Medicine*, vol. 1, pp. 1-24, 2011. [CrossRef] [Google Scholar] [Publisher Link]

[3] Mark W. Bondi, Emily C. Edmonds, and David P. Salmon, "Alzheimer's Disease: Past, Present, and Future," *Journal of the International Neuropsychological Society*, vol. 23, no. 9-10, pp. 818-831, 2017. [CrossRef] [Google Scholar] [Publisher Link]

[4] Marcos Vinícius Ferreira Silva et al., "Alzheimer's Disease: Risk Factors and Potentially Protective Measures," *Journal of Biomedical Science*, vol. 26, pp. 1-11, 2019. [CrossRef] [Google Scholar] [Publisher Link]

[5] Marta Crous-Bou et al., "Alzheimer's Disease Prevention: from Risk Factors to Early Intervention," *Alzheimer's Research & Therapy*, vol. 9, pp. 1-9, 2017. [CrossRef] [Google Scholar] [Publisher Link]

[6] Elizabeth Joe, and John M. Ringman, "Cognitive Symptoms of Alzheimer's Disease: Clinical Management and Prevention," *British Medical Journal*, vol. 367, 2019. [CrossRef] [Google Scholar] [Publisher Link]

[7] J. Mendiola-Precoma et al., "Therapies for Prevention and Treatment of Alzheimer's Disease," *Biomed Research International*, vol. 2016, pp. 1-17, 2016. [CrossRef] [Google Scholar] [Publisher Link]

[8] George Crisan et al., "Radiopharmaceuticals for PET and SPECT Imaging: A Literature Review over the Last Decade," *International Journal of Molecular Sciences*, vol. 23, no. 9, pp. 1-52, 2022. [CrossRef] [Google Scholar] [Publisher Link]

[9] Sandip Basu et al., "The Basic Principles of FDG-PET/CT Imaging," *PET Clinics*, vol. 9, no. 4, pp. 355-370, 2014. [CrossRef] [Google Scholar] [Publisher Link]

[10] Ashwini Prem Kumar et al., "Neuronal PET Tracers for Alzheimer's Disease," *Biochemical and Biophysical Research Communications*, vol. 587, pp. 58-62, 2022. [CrossRef] [Google Scholar] [Publisher Link]

[11] Lucas Porcello Schilling et al., "Imaging Alzheimer's Disease Pathophysiology with PET," *Dementia & Neuropsychologia*, vol. 10, no. 2, pp. 79-90, 2016. [CrossRef] [Google Scholar] [Publisher Link]

[12] Charles Marcus, Esther Mena, and Rathan M. Subramaniam, "Brain PET in the Diagnosis of Alzheimer's Disease," *Clinical Nuclear Medicine*, vol. 39, no. 10, pp. e413-e426, 2014. [CrossRef] [Google Scholar] [Publisher Link]

[13] N. Sadeghi et al., "Automatic Classification of Alzheimer's Disease vs. Frontotemporal Dementia: A Spatial Decision Tree Approach with FDG-PET," *2008 5th IEEE International Symposium on Biomedical Imaging: From Nano to Macro*, Paris, France, pp. 408-411, 2008. [CrossRef] [Google Scholar] [Publisher Link]

[14] Silvia Paola Caminiti et al., "FDG-PET and CSF Biomarker Accuracy in Prediction of Conversion to Different Dementias in a Large Multicentre MCI Cohort," *NeuroImage Clinical*, vol. 18, pp. 167-177, 2018. [CrossRef] [Google Scholar] [Publisher Link]

[15] Qing Li et al., "Classification of Alzheimer's Disease, Mild Cognitive Impairment, and Cognitively Unimpaired Individuals Using Multi-Feature Kernel Discriminant Dictionary Learning," *Frontiers in Computational Neuroscience*, vol. 11, pp. 1-14, 2018. [CrossRef] [Google Scholar] [Publisher Link]

[16] Liqun Kuang et al., "Metabolic Brain Network Analysis of FDG-PET in Alzheimer's Disease Using Kernel-Based Persistent Features," *Molecules*, vol. 24, no. 12, pp. 1-14, 2019. [CrossRef] [Google Scholar] [Publisher Link]

[17] Sebastian Palmqvist et al., "Detailed Comparison of Amyloid PET and CSF Biomarkers for Identifying Early Alzheimer Disease," *Neurology*, vol. 85, no. 14, pp. 1240-1249, 2015. [CrossRef] [Google Scholar] [Publisher Link]

[18] Bradley T. Wyman et al., "Standardization of Analysis Sets for Reporting Results from ADNI MRI Data," *Alzheimer's Dementia*, vol. 9, no. 3, pp. 332-337, 2013. [CrossRef] [Google Scholar] [Publisher Link]

[19] Krzysztof J. Gorgolewski et al., "The Brain Imaging Data Structure, A Format for Organizing and Describing Outputs of Neuroimaging Experiments," *Scientific Data*, vol. 3, 2016. [CrossRef] [Google Scholar] [Publisher Link]

[20] Karl J. Friston et al., *Statistical Parametric Mapping: The Analysis of Functional Brain Images*, 1st ed., Elsevier, 2007. [Google Scholar] [Publisher Link]

[21] Benjamin A Thomas et al., "PETPVC: A Toolbox for Performing Partial Volume Correction Techniques in Positron Emission Tomography," *Physics in Medicine & Biology*, vol. 61, no. 22, 2016. [CrossRef] [Google Scholar] [Publisher Link]

[22] Andrew Hoopes et al., "SynthStrip: Skull-Stripping for any Brain Image," *NeuroImage*, vol. 260, 2022. [CrossRef] [Google Scholar] [Publisher Link]

[23] Edmund T. Rolls et al., "Automated Anatomical Labelling Atlas 3," *NeuroImage*, vol. 206, 2020. [CrossRef] [Google Scholar] [Publisher Link]

[24] Fabian Pedregosa et al., "Scikit-Learn: Machine Learning in Python," *Journal of Machine Learning Research*, vol. 12, pp. 2825-2830, 2011. [Google Scholar] [Publisher Link]